Chemical Engineering Journal 468 (2023) 143543

Contents lists available at ScienceDirect

Chemical Engineering Journal

journal homepage: www.elsevier.com/locate/cej

Experimental evaluation of an indirectly-irradiated packed-bed solar thermochemical reactor for calcination–carbonation chemical looping

Lifeng Li [a,1], Alireza Rahbari [a,1], Mahdiar Taheri [a], Roelof Pottas [a], Bo Wang [a,b], Morteza Hangi [a], Leanne Matthews [c], Lindsey Yue [a], José Zapata [a,d], Peter Kreider [a], Alicia Bayon [e], Chi-Hwa Wang [f], Terrence W. Simon [c], Joe Coventry [a], Wojciech Lipiński [g,*]

[a] School of Engineering, The Australian National University, Acton, ACT, 2601, Australia
[b] NUS Environmental Research Institute, National University of Singapore, 5A Engineering Drive 1, Singapore 117411, Singapore
[c] Department of Mechanical Engineering, University of Minnesota, 111 Church Street South East, Minneapolis, MN 55455, USA
[d] IT Power Australia, Turner, ACT, 2602, Australia
[e] Institute of Catalysis and Petrochemistry—Consejo Superior de Investigaciones Científicas (CSIC), Calle Marie Curie, 2, Madrid, 28049, Spain
[f] Department of Chemical and Biomolecular Engineering, National University of Singapore, 4 Engineering Drive 4, 117585, Singapore
[g] Polna 1a, 05-600 Grójec, Poland

ARTICLE INFO

Keywords:
Solar chemistry
High temperature
Calcium oxide
Carbon capture
Energy storage

ABSTRACT

The two-step calcium oxide based calcination–carbonation cycle is studied for carbon dioxide capture and solar thermochemical energy storage applications. An indirectly-irradiated packed-bed solar thermochemical reactor is experimentally evaluated using simulated high-flux solar irradiation provided by a multi-source solar simulator. Experimental runs include a single calcination reaction step as well as single and multiple (up to four) consecutive calcination–carbonation cycles. The samples are characterised using scanning electron microscopy (SEM) and X-ray diffraction (XRD). The reactor temperature peaked at 1,035°C. The average solar-to-chemical conversion efficiency, defined as the ratio of heat consumed by the reaction to radiant heat supplied to the reactor, was found to be between approximately 1.3% and 8.6% for the five performed experimental runs. The necessary advancements to the presented reactor design identified during the experimental campaign include improvements in thermomechanical characteristics of ceramic and metallic parts of the reactor to prevent fast mechanical and chemical degradation, application of more robust high-temperature reaction chamber seals, and optimisation of reactor geometry and gas flow patterns towards spatially more uniform thermal conditions and chemical reaction rates.

1. Introduction

The two-step calcium-oxide (CaO) based calcination–carbonation chemical looping has been studied for carbon dioxide (CO_2) capture and high-temperature thermochemical energy storage applications [1–3]. The process involves an endothermic calcination reaction of calcium carbonate ($CaCO_3$) and an exothermic carbonation reaction of CaO with CO_2 [4–6],

$$\text{Calcination}: \quad CaCO_3 \rightarrow CaO + CO_2, \quad \Delta\bar{h}^{\circ}_{\text{calc},298\,\text{K}} = 178\,\text{kJ mol}^{-1}, \tag{1a}$$

$$\text{Carbonation}: \quad CaO + CO_2 \rightarrow CaCO_3, \quad \Delta\bar{h}^{\circ}_{\text{carb},298\,\text{K}} = -178\,\text{kJ mol}^{-1}. \tag{1b}$$

Under a pure CO_2 atmosphere at 1 bar, the calcination reaction, Eq. (1a), proceeds spontaneously at temperatures above 900°C. $CaCO_3$ calcination has been extensively studied as the product of this reaction has many industrial applications [7]. The carbonation reaction proceeds at a lower temperature of about 650°C. Compared with other carbonate materials such as strontium carbonate ($SrCO_3$) [8], barium carbonate ($BaCO_3$) [9], and manganese carbonate ($MnCO_3$) [10], the commonly occurring calcium carbonate has the benefits of relatively high energy storage density (1,657 kJ kg^{-1}), CO_2 capture capacity, and low cost (about 0.08 AUD$ kg^{-1}) [11]. The kinetics of $CaCO_3$ calcination and CaO carbonation reactions have been extensively studied [4,12–19]. Examples of studies of thermal transport phenomena in calcination and carbonation reaction systems for solar thermochemical applications include an analysis of transient radiative heat transfer in a suspension of small particles undergoing calcination [20], an analysis of combined heat transfer in a packed bed of large particles undergoing

* Corresponding author.
E-mail address: wsl@member.fsf.org (W. Lipiński).
[1] Equally contributing authors.

https://doi.org/10.1016/j.cej.2023.143543
Received 11 November 2022; Received in revised form 21 April 2023; Accepted 13 May 2023
Available online 18 May 2023

Nomenclature

Abbreviations

ANU	The Australian National University
CFD	computational fluid dynamics
CMOS	complementary metal oxide semi-conductor
CST	concentrating solar thermal
GHG	greenhouse gas
HFSS	high-flux solar simulator
MFCs	mass flow controllers
PXRD	powder X-ray diffraction
SEM	scanning electron microscopy
TGA	thermogravimetric analyses
XRD	X-ray diffraction

Greek letters

η	efficiency
ν	stoichiometric coefficient
ρ	density, $\mathrm{kg\,m^{-3}}$

Latin letters

$\bar{c}_p$	specific heat capacity, $\mathrm{J\,mol^{-1}\,K^{-1}}$
$\bar{M}$	molar mass, $\mathrm{kg\,mol^{-1}}$
$\Delta\bar{h}$	molar enthalpy change, $\mathrm{J\,mol^{-1}}$
$\dot{m}$	mass flow rate, $\mathrm{kg\,s^{-1}}$
$\dot{n}$	molar flow rate, $\mathrm{mol\,s^{-1}}$
$\dot{Q}$	heat rate, W
$\dot{V}$	volumetric flow rate, $\mathrm{l\,min^{-1}}$
f	gas leakage ratio
m	mass, kg
p	partial pressure, Pa
Q	heat, J
T	temperature, K
t	time, s
X	extent of reaction
y	molar fraction

Subscripts

calc	calcination
carb	carbonation
eg	exhaust gases
i	insulation, inlet
in	incident
max	maximum
o	outlet
r	reaction
s-c	solar-to-chemical
tot	total

calcination [21], and analyses of combined heat and mass transfer in single particles undergoing calcination [22–24] and cyclic calcination and carbonation [12,17,25]. Transient temperature and thermal stress profiles in single $CaCO_3$ particles undergoing rapid heating under concentrated solar irradiation were studied in [26]. An overview of thermal transport models for carbonate-based reacting systems is given in [27]. Further discussions of materials, processes, and systems for carbonate-based calcination–carbonation reactions for CO_2 capture or thermochemical energy storage can be found in [28–31].

The endothermic calcination reaction can be driven via concentrating solar thermal (CST) energy as a viable source of process heat [32–35]. In CST systems, optical mirrors concentrate solar rays onto a small target area. The dominant CST technologies include: (*i*) parabolic trough collectors suitable for low-temperature heat applications, in the range of 150°C to 350°C; (*ii*) central receiver systems producing molten salts or superheated steam at medium receiver temperatures of around 565°C due to the limitation of the molten salts (modified salts can stand 700°C [36]); (*iii*) parabolic dish collectors providing receiver temperatures over 700°C; and (*iv*) linear Fresnel collectors reaching temperatures above 500°C. The point-focusing optical concentrators, including central receiver systems and parabolic dish collectors, are capable of providing the highest concentration ratios for high-temperature applications [37–39]. Examples of efforts to increase the receiver temperature in central receiver systems include the work at HelioHeat (>1,000°C) and Synhelion (>1,550°C) [40]. Solar-driven $CaCO_3$-based chemical looping is an attractive option due to low-pressure operation, less-expensive reactor materials, and more effective use of sorbent per unit mass for capturing CO_2 [41]. The integration of CST with calcination–carbonation chemical looping has been investigated for CO_2 capture [1,32,42] or thermochemical energy storage applications [33,34,43]. In recent years, the feasibility of solar calcium looping and the integration of this process into a cement production plant has been demonstrated [31,44–46]. The reactor design was at the focus of these studies due to the challenges induced by the reaction conditions and material properties.

A solar reactor is the key component of a solar thermochemical system. It converts concentrated solar radiation into chemical energy [47–49]. Although chemical kinetics and thermal transport phenomena of the CaO-based calcination–carbonation reaction have been extensively studied, the integration of the reactions with concentrated solar thermal energy in a solar reactor remains challenging due to inherent complexities associated with the design and operation of high-temperature solar reactors providing distinct conditions for each of the reactions (1a) and (1b). Implementation of the reactions in a solar reactor much exceeds the level of technical complexities typically encountered in studies using thermogravimetric analysers (TGAs) or electric furnace because: (*i*) the temperature control in a solar reactor is more difficult than in a TGA or an electric furnace; (*ii*) the amount of reacting materials used in a solar reactor is higher than in a TGA or an electric furnace; (*iii*) direct absorption of sunlight by $CaCO_3$ and CaO is relatively low. According to the mode of solar irradiation, solar reactors can be classified as directly- and indirectly-irradiated. Although directly-irradiated solar reactors theoretically offer more efficient heat transfer to chemical reactions, their inherent drawbacks are due to (*i*) the need for a quartz window to confine the reactants and (*ii*) large temperature non-uniformity in the cavity [50,51]. To alleviate issues with window contamination and overheating, gas flow protection and cooling systems have been proposed and demonstrated. For more details, see the recent study by Wang et al. [52] and the literature cited therein. In the case of indirectly-irradiated solar reactors, these issues are avoided at the expense of increased irreversibilities due to heat transfer through opaque walls and other media.

Solar reactor configurations for the solar calcination reaction reported previously include fluidised beds [45,55–58], cyclones (vortex-type reactors) [59], rotary kilns [44,60,61], and packed beds [53]. Solar fluidised-bed calciners offer high heat and mass transfer rates due to intense mixing of solid–gas reactants, which in turn results in more uniform temperature and chemical reaction rate distributions. Fluidised-bed calciners can achieve high extents of the calcination reaction, reaching 80%–100%. However, particle attrition, issues with fluidisation of particles with broad size distribution, and a complex mechanical structure are the key challenges to the design of solar fluidised-bed calciners [45,55,56]. Similarly, the extent of the calcination reaction in solar cyclone calciners can attain high values, up to 85% [62]. A key technological challenge is material clogging and

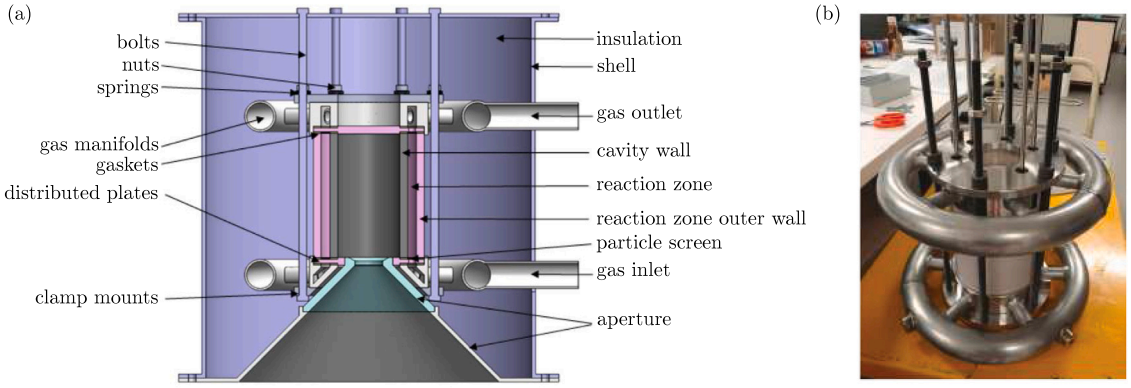

Fig. 1. The indirectly-irradiated packed-bed solar thermochemical reactor for calcination–carbonation chemical looping: (a) schematic of the cross-sectional view (adapted from [53]) and (b) photograph of the assembled inner structure. More details of the reactor design and assembling process can be found in [53,54].

a large amount of gas required to carry particles. Typically, particles smaller than 50 μm are used in solar fluidised-bed and cyclone calciners [31]. Rotary kiln calciners have the flexibility to accommodate particles with a broader size distribution. The extent of the calcination reaction ranges from 24% to 98%—the upper threshold is achievable with suitable mixing of particles [44,55,60,63,64]. However, large temperature gradients along the reactor length occur [51]. The reported values of the solar-to-chemical energy conversion efficiency of solar rotary-kiln reactors range from 4.5% to a maximum of 35% [60,63,64]. The solar CaO looping can be conducted in: (i) a two-reactor configuration as the most conventional system, in which solid particles are cycled between two separate reactors being a solar calciner and a non-solar carbonator and (ii) a single-reactor configuration, which allows both reactions (1a) and (1b) to proceed in one reactor by adjusting the gas composition and solar input as required by the carbonation and calcination steps. Single-reactor configurations developed for solar CaO looping include a packed bed reactor [54] and a fluidised bed reactor [42]. The fluidised-bed reactor presented in the latter study is the only solar reactor demonstrated to date for cyclic CaO-based calcination–carbonation reactions [42]. In this reactor, CaO carbonation and $CaCO_3$ calcination were carried out at 365–400°C and 800–875°C, respectively. The calcination reaction was carried out under a pure Ar atmosphere. Single-reactor configurations were adopted for realising other cyclic thermochemical processes in which the switch between two cycle steps was realised by (i) moving reactor parts [65–68] or (ii) varying sweeping gases [69,70]. Alternative configurations are arrays of two or more stationary reactors [71,72], or trains of moving reactors [73]. In the multi-reactor systems, individual reactors are subjected to alternating solar irradiation and other external conditions as appropriate for different stages of multi-step thermochemical cycles.

Solar packed-bed reactors offer several advantages to carry out cyclic calcination–carbonation reactions as compared to the reactor types discussed above. The two reactions can be carried out sequentially in the same reactor, mitigating the need for transferring solids between separate calcination and carbonation reactors or for alternating the concentrated solar irradiation between separate reactors. No cyclic calcination–carbonation process demonstrated in a solar packed-bed reactor has been reported in the literature to date. Here, we present design and experimental evaluation of a 2-kW_{th} indirectly-irradiated solar packed-bed reactor prototype for the CaO-based cyclic calcination–carbonation reactions [53,54,74]. The reactor is shown in Fig. 1. It features a dual concentric cylindrical cavity. The inner cavity serves as the radiation receiver while the annular cylindrical cavity is the reaction chamber containing reactive particles. Thermodynamic and heat transfer analyses underpinning the design of this reactor were previously reported in [54,75]. The experimental evaluation is accomplished with simulated high-flux solar irradiation provided by the multi-source high-flux solar simulator (HFSS) at the Australian National University (ANU) [76–78]. The reactor performance is experimentally evaluated for: (*i*) a single calcination reaction step, (*ii*) a single calcination–carbonation cycle, and (*iii*) multiple consecutive calcination–carbonation cycles. The evaluated characteristics are temperature, rates, and extents of the calcination and carbonation reactions, solar-to-chemical energy conversion efficiency, and mechanical stability of the reactor. The reaction kinetics and material characteristics were comprehensively studied using TGA, scanning electron microscope (SEM), and X-ray diffraction (XRD) with the solid reactants and products used in the solar reactor experiments.

2. Experimental

The two-step calcium oxide based calcination–carbonation cycle is conducted in the solar thermochemical reactor setup shown in Fig. 2. The setup consists of the ANU HFSS, the indirectly-irradiated packed-bed thermochemical reactor, measurement instrumentation, and auxiliary equipment.

2.1. High-flux solar simulator

The ANU HFSS consists of 18 radiation modules each consisting of a 2.5 kW_e xenon short-arc lamp, a truncated ellipsoidal reflector, a cooling fan, and electronics [76]. The orientations and positions of these modules were determined from geometrical relations including the rim angle, the number of radiation modules, the number of rows, the reflector radius, and the inter-module spacing parameter. The eccentricity of the ellipsoidal reflectors was chosen such that the reflector intercepts the radiation emitted by the lamp [76,79]. This facility provides radiative power and mean radiative flux up to 10.6 kW and 3.8 $MW\,m^{-2}$ on a 60-mm diameter circular flat target [78].

2.2. Solar reactor

Fig. 1 shows the schematic of the indirectly-irradiated packed-bed solar thermochemical reactor for CaO-based calcination–carbonation chemical looping. The reactor comprises the inner cylindrical cavity, the outer annular cavity, the top and bottom distributor plates, particle screens, gas manifolds, and clamping mounts. These components are assembled using six long bolts (high-tensile steel), 30 springs, and 1 nut on each bolt to provide the clamping force. A dense fibre material (Nefalit 11, $\rho = 1.1\,g\,cm^{-3}$) is used as gaskets to seal the space between the upper and bottom surfaces of the cavity walls and the manifolds. The inner wall of the cavity is made of silicon carbide (SiC, CoorsTek Ultra SiC™) due to: (*i*) high optical absorptance to capture the solar irradiation, (*ii*) high thermal conductivity (150 $W\,m^{-1}\,K^{-1}$ at 20°C) for transferring the absorbed heat to the particles, and (*iii*) excellent resistance to high temperature and thermal shock. The outer wall of the

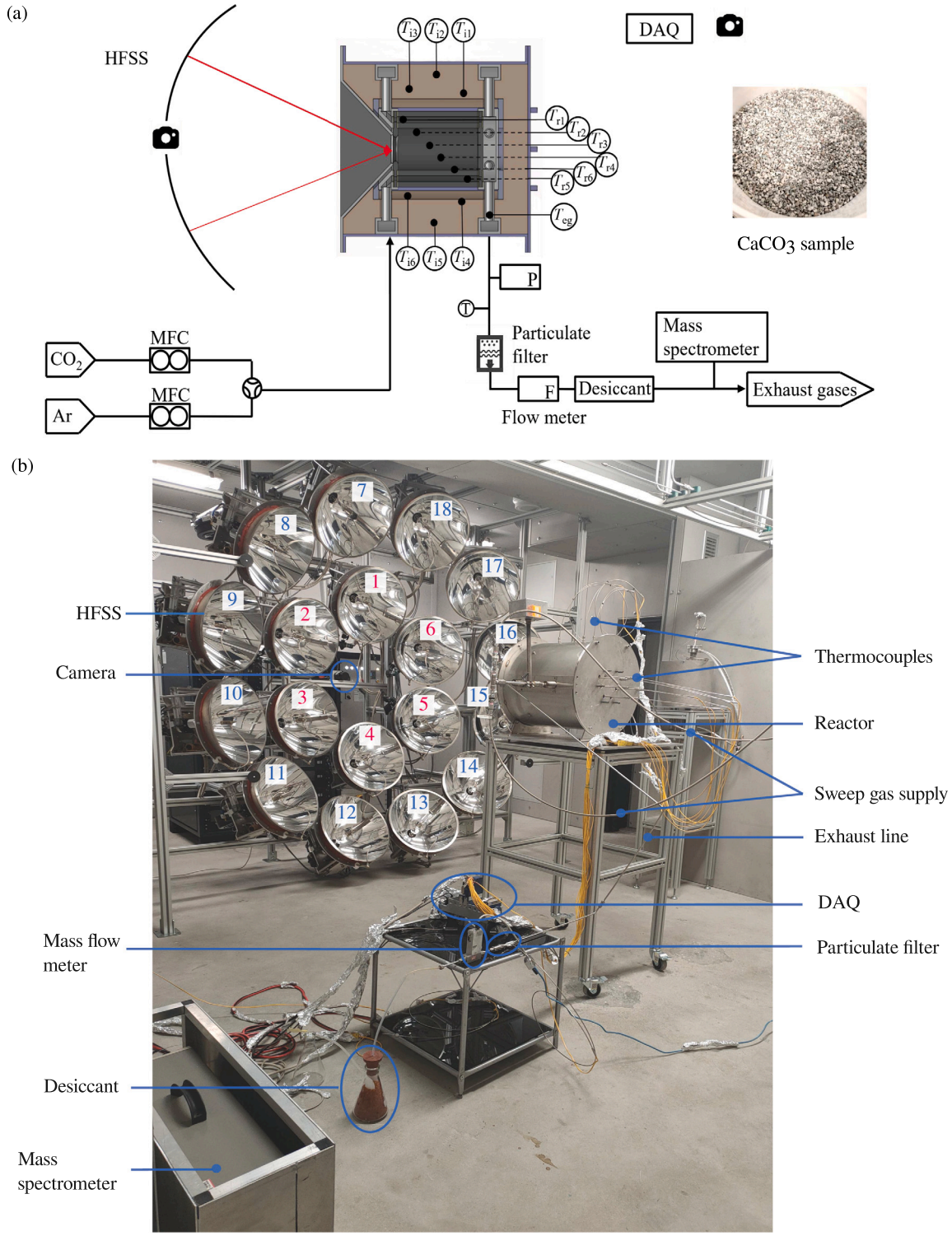

Fig. 2. Experimental setup consisting of the ANU HFSS, the assembled solar reactor, the measurement instrumentation, and auxiliary equipment including data acquisition (DAQ): (a) schematic diagram and (b) photograph. In this work, radiation modules #1–6 of the HFSS (labelled in red) are used.

cavity—containing a packed bed of reacting particles ($CaCO_3$ or CaO)—is made of mullite which has a relatively lower thermal conductivity (20 $W\,m^{-1}\,K^{-1}$ at 20°C) to reduce the thermal losses from the reaction zone. The distributor plates form the top and bottom walls of the reactor cavity facilitate gas flow from the plenum into the reaction zone [54]. The cavity containing reacting particles has 16 cm height, 9 cm inner diameter, and 11.3 cm outer diameter. The aperture has a height of 15 cm, inner diameter of 3.57 cm, and outer diameter of 32 cm. The distributor plates are made of mullite while the other parts, including the particle screens, gas manifolds, and clamping mounts, are

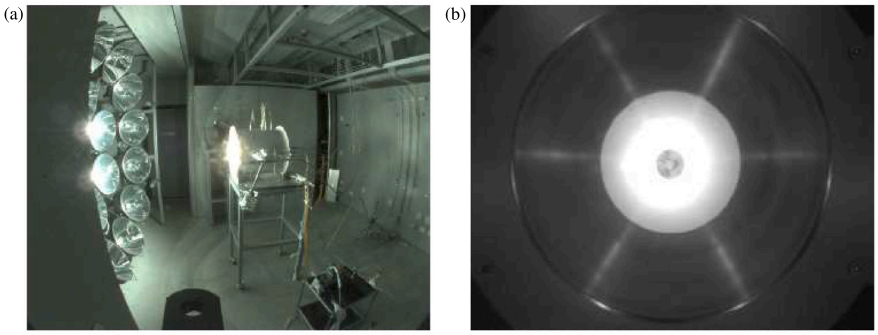

Fig. 3. Photographs of the solar calcination–carbonation reactor during an on-flux test using simulated solar irradiation provided by the ANU HFSS: (a) the HFSS and reactor setup shot by the camera at the side wall, and (b) the reactor aperture shot by the camera at the centre of HFSS radiation modules.

made of Inconel 625 that can sustain temperatures up to 1,290°C. More details on the reactor design and the process of assembling can be found in [53,54].

2.3. Instrumentation

The reactor setup is equipped with 14 type-K class-1 thermocouples, among which six are located inside the reacting-particle bed at various depths (T_{r1}–T_{r6}), one is located in the exhaust gas flow leaving the reaction zone (T_{eg}), six are located inside the insulation (T_{i1}–T_{i6}), and one is located at the far end of the exhaust gas line before entering the particulate filter (see Fig. 2a). The thermocouple locations were selected to ensure that the maximum temperature does not exceed 1,100°C, as limited by the reactor materials, to measure reactor temperature distribution, to obtain representative temperature of the reaction bed, and to evaluate thermal energy losses from the reactor. The thermocouples are sealed and attached to the reactor using Swagelok fittings.

The flow of purge gases supplied to the reactor ($\dot{V}_{CO_2,i}$ and $\dot{V}_{Ar,i}$) is controlled by mass flow controllers (MFCs) (Bronkhurst, F-201CV-10K-RGD-22-Z for CO_2 and F-201CV-5K0-RGD-22-V for Ar). The mass flow rate and composition of the gases leaving the reaction zone are measured by a mass flow meter (Bronkhurst, F-111B-10K-RGD-22-V) and a mass spectrometer (Stanford Research System, QMS 100 Series Gas Analyser) [80], respectively. To protect the mass flow meter and the mass spectrometer, a Swagelok 7 μm in-line particle filter is connected to the exhaust gas line to remove the fine powder created by particle attrition. The exhaust gas pipe has a length of approximately 2 m from the reactor outlet to the entry point of a particulate filter, allowing for the cooling of the hot exhaust gases. A thermocouple is employed to monitor the temperature of the exhaust gases before entering the particle filter. Additionally, a silica gel desiccant is placed in the exhaust gas line before the mass spectrometer to absorb the moisture released by the particles during the heat-up phase.

Two cameras are installed in the HFSS and experimental rooms to monitor the experiments with the reactor: (*i*) a complimentary metal-oxide semi-conductor (CMOS) type, colour camera (Basler acA1300-60gc, 12 pixel bit-depth, 1.3 MP) on the side wall, which provides the side view of the reactor setup; and (*ii*) a CMOS-type, monochromatic camera (Basler acA1920-50gm, 12 pixel bit-depth, 2.3 MP) equipped with a manual zoom lens (Computar M6Z1212) and neutral density filters (≈0.012% transmission) at the centre of the HFSS radiation modules, which provides the front view of the reactor setup. Fig. 3 shows images taken by the cameras during an example experimental run.

The cameras, MFCs, mass flow meter and the thermocouples are connected directly to a desktop computer, and the data are recorded and visualised using a LabVIEW program. The HFSS and mass spectrometer are controlled using vendor-provided software.

2.4. Experimental procedure

In this work, up to six radiation modules in the HFSS inner row (#1–6 in Fig. 2b) are used for the solar reactor testing. Prior to using the HFSS for the reactor testing, the reflectors and lamps were optically aligned and radiative flux and power distributions in the focal area were characterised using a combined methodology of close-range photogrammetry and radiometry techniques [78,81]. The HFSS reflectors and lamps were aligned to maximise the radiative power entering through the reactor aperture while minimising the spillage loss outside the reactor aperture. The common radiometric approach was applied to measure the radiative flux output by employing two mobile water-cooled Lambertian targets, a heat flux gauge, and a complementary metal oxide semi-conductor (CMOS) camera equipped with neutral-density filters [78,81].

For each experimental run, the experimental procedure starts with pressure tests of the assembled reactor using compressed nitrogen (N_2) and a pressure gauge connected to the reactor inlet and outlet, respectively. Gas leakage locations are identified using soap water, which are subsequently sealed using alumina cement (ZIRCAR Alumina Cement, Type AL-CEM, 99% Al_2O_3 and 0.92% SiO_2 (wt%)) with melting point above 1,870°C. The space between the reactor outer cavity wall and the reactor outer housing is insulated with ceramic fibre blanket (Morgan Advanced Materials, Superwool Xtra blankets, thermal conductivity of 0.16 $W\,m^{-1}\,K^{-1}$ at 600°C, melting point of 1,650°C). The assembled reactor is precisely positioned relative to the HFSS by laser-aligning the centre of the reactor aperture with the centre of the focal spot of the HFSS. The operation of the reactor during the calcination and carbonation steps is controlled by changing the sweep gas composition and the radiative input to the reactor. The inlet gas for both calcination and carbonation reactions is a mixture of CO_2 and Ar, with proportions adjusted specifically for each experiment.

The six radiation modules are operated at the arc currents of 70 A, 85 A, and 100 A, to provide the total radiative power of 1.2 kW, 1.6 kW, and 2.0 kW, respectively, and average radiative flux of 1,167.9 $kW\,m^{-2}$, 1,506.7 $kW\,m^{-2}$, and 1,914.3 $kW\,m^{-2}$, respectively. During the experiments, the radiative power input to the reactor is adjusted by modifying the number and/or the currents of the HFSS lamps to maintain the desired calcination or carbonation temperatures. To reduce the thermal shock to the reactor components, the following strategy is used during the ramp-up/ramp-down stages. The HFSS lamps are sequentially turned on, each at arc current of 70 A, at 10 min intervals. Next, the arc currents are increased to 100 A sequentially and at the same time intervals. During the shut-down stage, the process is reversed, i.e. first the arc current is sequentially reduced to an intermediate value of 70 A or 85 A, followed by turning off the lamps sequentially at 10 min intervals. The sorbent particles are extracted from the reactor and weighed for the determination of the reaction extent and the subsequent materials characterisation when the reactor cools to room temperature, typically within 8–12 h after completion of an on-flux experimental run.

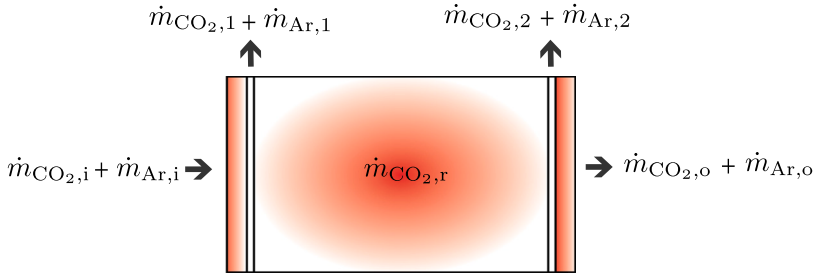

Fig. 4. Gas mass flows through the reactor system. $\dot{m}_{CO_2,i}$ and $\dot{m}_{Ar,i}$ are mass flow rates of CO_2 and Ar at the reactor gas inlet, respectively; $\dot{m}_{CO_2,1}$ and $\dot{m}_{Ar,1}$ are mass flow rates of the leaked CO_2 and Ar before the gases reach the reaction zone, respectively; $\dot{m}_{CO_2,r}$ is the change of mass flow rate of CO_2 due to the chemical reaction in the reaction zone; $\dot{m}_{CO_2,2}$ and $\dot{m}_{Ar,2}$ are mass flow rates of the leaked CO_2 and Ar after the reaction zone, respectively; and $\dot{m}_{CO_2,o}$ and $\dot{m}_{Ar,o}$ are mass flow rates of the CO_2 and Ar at the reactor outlet, respectively.

2.5. Materials characterisation

The limestone (95% $CaCO_3$, 3.5% $MgCO_3$, and 1.5% acid-insoluble contents; naturally occurring marble) particles (1.4–5.6 mm diameter) were obtained from Omya Australia Pty Limited [82] (see Fig. 2a). Thermogravimetric analysis (TGA, Netzsch STA 449) is conducted to study kinetics of calcination and carbonation using the received sample material. The effects of calcination and carbonation temperatures, heating rate, gas atmosphere composition and duration of calcination and carbonation steps on reaction extents and rates are investigated to guide the preparation of the on-flux solar reactor tests in the HFSS. To study the crystal structure of the powder, X-ray diffraction (PXRD) patterns are recorded using a D2 Phaser (Bruker, USA) equipped with Cu Kα radiation of average wavelength 1.5406 Å. A scanning electron microscope (SEM) (Zeiss UltraPlus analytical FESEM) equipped with an in-lens secondary electron detector (3 kV accelerating voltage) is used to study the microstructure of the particles. Particles are mounted in resin epoxy and polished to investigate their cross sections. Prior to imaging, the polished samples are coated with platinum.

3. Analysis

A steady-state model based on mass and energy balance equations is developed to evaluate the performance metrics of the reactor. Fig. 4 depicts the input and output mass flows of gases entering the reactor (controlled and recorded by the MFCs), leaking before and after the reaction zone, released/absorbed in the chemical reactions, and leaving the reactor in the exhaust stream. The gas leakage ratios before and after the reaction zone, $\dot{f}_1$ and $\dot{f}_2$, respectively, are defined as

$$\dot{f}_1 = \frac{\dot{m}_{CO_2,1} + \dot{m}_{Ar,1}}{\dot{m}_{CO_2,i} + \dot{m}_{Ar,i}}, \tag{2}$$

$$\dot{f}_2 = \frac{\dot{m}_{CO_2,2} + \dot{m}_{Ar,2}}{(\dot{m}_{CO_2,i} + \dot{m}_{Ar,i}) - (\dot{m}_{CO_2,1} + \dot{m}_{Ar,1}) + \dot{m}_{CO_2,r}}. \tag{3}$$

Assuming a uniform distribution of CO_2 and Ar gases at any reactor location, it is possible to calculate the mass flow rates of CO_2 and Ar leaked before and after the reaction zone as

$$\dot{m}_{CO_2,1} = \dot{f}_1 \dot{m}_{CO_2,i}, \tag{4}$$

$$\dot{m}_{CO_2,2} = \dot{f}_2 \left[(1-\dot{f}_1)\dot{m}_{CO_2,i} + \dot{m}_{CO_2,r}\right], \tag{5}$$

$$\dot{m}_{Ar,1} = \dot{f}_1 \dot{m}_{Ar,i}, \tag{6}$$

$$\dot{m}_{Ar,2} = \dot{f}_2 (1-f_1)\dot{m}_{Ar,i}. \tag{7}$$

Based on the mass balance of CO_2 and Ar gases, the mass flow rates of CO_2 and Ar leaving the reactor through the exhaust line are

$$\dot{m}_{CO_2,o} = (1-\dot{f}_2)\left[(1-\dot{f}_1)\dot{m}_{CO_2,i} + \dot{m}_{CO_2,r}\right], \tag{8}$$

$$\dot{m}_{Ar,o} = (1-\dot{f}_2)(1-\dot{f}_1)\dot{m}_{Ar,i}. \tag{9}$$

The total masses of CO_2 and Ar leaving the reactor through the exhaust line are obtained by integrating the above mass flow rates over the duration of an experimental run, Δt,

$$m_{CO_2,o} = (1-\bar{f}_2)\left[(1-\bar{f}_1)m_{CO_2,i} + m_{CO_2,r}\right] \tag{10}$$

$$m_{Ar,o} = (1-\bar{f}_2)(1-\bar{f}_1)m_{Ar,i}, \tag{11}$$

where it has been assumed that $\dot{f}_1$ and $\dot{f}_2$ do not change during an experimental run, $\dot{f}_1 = \bar{f}_1$ and $\dot{f}_2 = \bar{f}_2$. Eqs. (10) and (11) can be used to derive $\bar{f}_1$ and $\bar{f}_2$, considering that

$$m_{CO_2,i} = \int \dot{m}_{CO_2,i}\mathrm{d}t = \int_{\Delta t} \rho_{CO_2}\dot{V}_{CO_2,i}\mathrm{d}t, \tag{12}$$

$$m_{Ar,i} = \int \dot{m}_{Ar,i}\mathrm{d}t = \int_{\Delta t} \rho_{Ar}\dot{V}_{Ar,i}\mathrm{d}t, \tag{13}$$

$$m_{CO_2,o} = \int \dot{m}_{CO_2,o}\mathrm{d}t = \int_{\Delta t} y_{CO_2}\rho_{CO_2}\dot{V}_{tot,o}\mathrm{d}t, \tag{14}$$

$$m_{Ar,o} = \int \dot{m}_{Ar,o}\mathrm{d}t = \int_{\Delta t} y_{Ar}\rho_{Ar}\dot{V}_{tot,o}\mathrm{d}t, \tag{15}$$

where $\dot{V}_{CO_2,i}$ and $\dot{V}_{Ar,i}$ are the volumetric flow rates of the CO_2 and Ar gases at the reactor gas inlet (controlled by MFCs); ρ_{CO2} and ρ_{Ar} are the densities of CO_2 and Ar at 25°C; $\dot{V}_{tot,o}$ is the total volumetric flow rate of the CO_2 and Ar mixture leaving the reactor through the exhaust line (measured by the mass flow meter); and y_{CO_2} and y_{Ar} are the molar fractions of CO_2 and Ar in the exhaust flow, calculated based on the partial pressures of CO_2 and Ar measured by the mass spectrometer.

The mass change of CO_2 attributed to chemical reactions, $m_{CO_2,r}$, is determined by weighing the sorbent particles used in the reactor before and after each on-flux test. Thus, $\bar{f}_1$ and $\bar{f}_2$ are derived as

$$\bar{f}_1 = 1 - \frac{m_{CO_2,o}m_{Ar,i} - m_{CO_2,i}m_{Ar,o}}{m_{CO_2,r}m_{Ar,i}}, \tag{16}$$

$$\bar{f}_2 = 1 - \frac{m_{CO_2,r}m_{Ar,o}}{m_{CO_2,o}m_{Ar,i} - m_{CO_2,i}m_{Ar,o}}. \tag{17}$$

Using Eq. (8), the mass and molar flow rates of CO_2 released/absorbed in the chemical reactions are obtained as

$$\dot{m}_{CO_2,r} = \frac{\dot{m}_{CO_2,o}}{(1-\bar{f}_2)} - (1-\bar{f}_1)\dot{m}_{CO_2,i}, \tag{18}$$

$$\dot{n}_{CO_2,r} = \frac{\dot{m}_{CO_2,r}}{\bar{M}_{CO_2}}, \tag{19}$$

where $\bar{M}_{CO_2}$ is the molar mass of CO_2.

The heat rate due to chemical reactions is calculated as

$$\dot{Q}_r = \Delta\bar{h}_T \dot{n}_{CO_2,r}, \quad \Delta\bar{h}_T = \Delta\bar{h}^{\circ}_{298\,K} + \int_{298\,K}^{T}\left(\sum_i \nu_i \bar{c}_{p,i}(T)\right)\mathrm{d}T, \tag{20}$$

where ν_i are stoichiometric coefficients of reactants and products i. The temperature-dependent specific heat capacities (in J $mol^{-1}K^{-1}$) of CaO, CO_2, and $CaCO_3$ are taken as [7,83,84]

$$\bar{c}_{p,CaO}(T) = 4.18\times10^{-3}T + 50.42 - 8.5\times10^{5}T^{-2}, \tag{21}$$

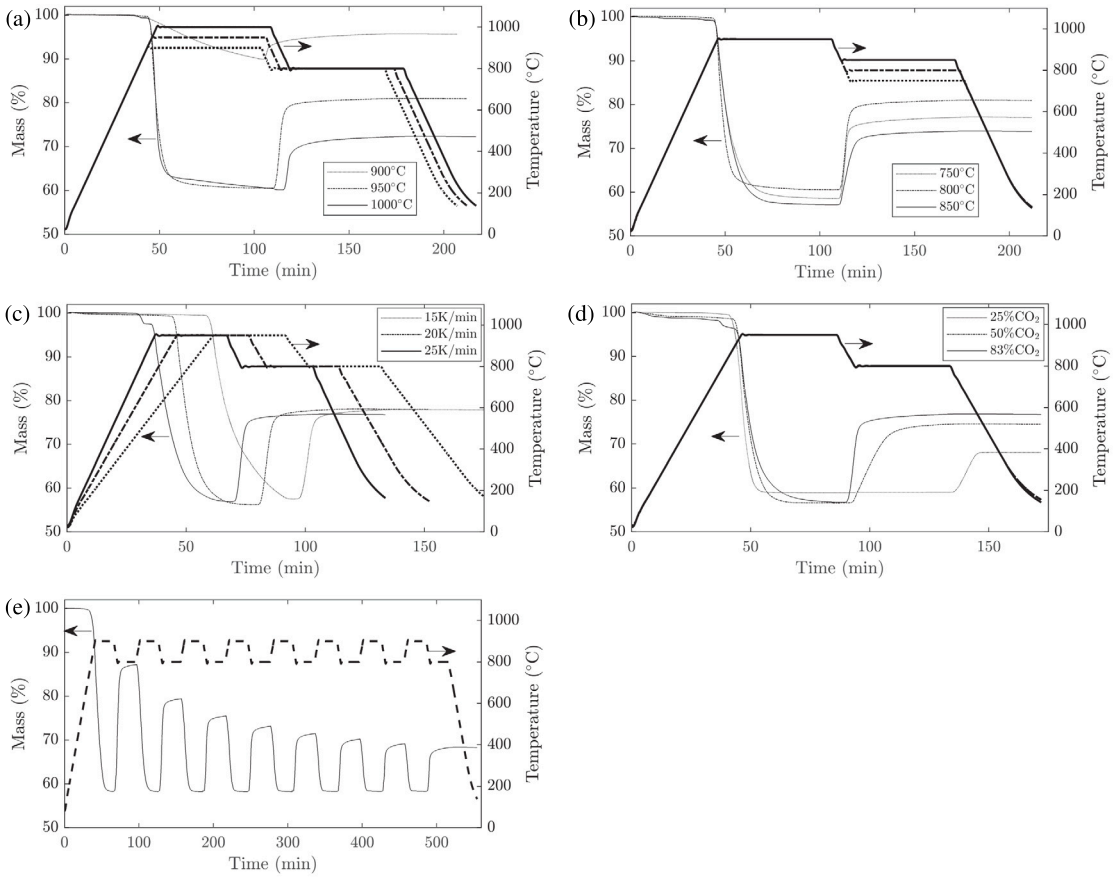

Fig. 5. Time evolution of the sample mass for the sorbent material—calcium carbonate undergoing (a–d) a single calcination–carbonation cycle and (e) multiple calcination–carbonation consecutive cycles. Baseline parameters are set as calcination temperature of 950°C, carbonation temperature of 800°C, heating rate of 20 K min^{-1}, and CO_2 molar fraction of 83% (100 ml min^{-1} CO_2 and 20 ml min^{-1} Ar). When one parameter is investigated, the other parameters are taken from the baseline set. The studied parameter sets include: (a) calcination temperatures of 900, 950, and 1,000°C, (b) carbonation temperatures of 750, 800, and 850°C, (c) heating rates of 15, 20, and 25 K min^{-1}, and (d) gas atmosphere with CO_2 molar fractions of 25%, 50%, and 83%.

$$\bar{c}_{p,\mathrm{CaCO_3}}(T) = 21.92\times10^{-3}T + 104.52 - 2.59\times10^{6}T^{-2}, \tag{22}$$

$$\bar{c}_{p,\mathrm{CO_2}}(T) = 4.37\times10^{-3}T + 51.13 - 1.47\times10^{6}T^{-2}. \tag{23}$$

In this study, $\Delta\bar{h}_T$ is evaluated using the average value of the temperatures measured by the six thermocouples placed inside the reaction zone.

The reactor performance is characterised using three metrics: (*i*) the average solar-to-chemical energy conversion efficiency during the calcination reaction step, $\bar{\eta}_{\mathrm{s-c}}$; (*ii*) the extent (degree) of calcination, $X_{\mathrm{r}}(t)$; and (*iii*) the temperature non-uniformity insider the reaction zone. They are defined as

$$\bar{\eta}_{\mathrm{s-c}} = \frac{Q_{\mathrm{r}}}{Q_{\mathrm{in}}} = \frac{\int_{\Delta t}\dot{Q}_{\mathrm{r}}\mathrm{d}t}{\int_{\Delta t}\dot{Q}_{\mathrm{in}}\mathrm{d}t}, \tag{24}$$

$$X_{\mathrm{r}}(t) = \frac{\int_0^t \dot{m}_{\mathrm{CaCO_3,r}}\mathrm{d}t}{m_{\mathrm{CaCO_3,0}}}, \tag{25}$$

$$\dot{m}_{\mathrm{CaCO_3,r}} = \dot{m}_{\mathrm{CO_2,r}}\frac{\bar{M}_{\mathrm{CaCO_3}}}{\bar{M}_{\mathrm{CO_2}}}, \tag{26}$$

where $m_{\mathrm{CaCO_3,0}}$ is the initial mass of the $CaCO_3$ particles used in the experiments, $\dot{m}_{\mathrm{CaCO_3,r}}$ is the mass of particles in the reaction zone after an experimental run of duration t, and $\dot{Q}_{\mathrm{in}}$ is the radiant energy input to the reactor.

4. Results and discussion

The reactor performance is experimentally evaluated for: (*i*) a single calcination reaction step, (*ii*) a single calcination–carbonation cycle, and (*iii*) multiple consecutive calcination–carbonation cycles. TGA tests of the $CaCO_3$ sample were carried out firstly to understand the reaction kinetics of the materials, which informs the operation of the reactor experiments.

4.1. Thermogravimetric analyses

Fig. 5 shows the effects of operating parameters including calcination temperature T_{calc}, carbonation temperature T_{carb}, heating rate, and CO_2 concentration on the reaction rate and extent. According to Fig. 5a, an optimal calcination temperature of 950°C (compared with 900°C and 1,000°C) is found, offering the best combined result of reaction extents for calcination and carbonation steps. The fast (chemistry-controlled) and slow (diffusion-controlled) regimes of carbonation kinetics are clearly observed. From Fig. 5b, the optimal carbonation temperature is found to be 800°C (compared with 750°C and 850°C). A lower temperature reduces the reaction rate, while a higher temperature promotes the formation of a solid blocking layer at the surface of particles that prevents CO_2 from contacting with CaO [12]. Fig. 5c shows that the calcination reaction starts when the temperature reaches approximately 920°C regardless of the heating rate. The heating rate is found to have negligible effects on the single calcination–carbonation cycle of the tested sorbent material. According to Fig. 5d, the onset temperature of carbonation reaction is dependent on CO_2 partial pressure—the lower the CO_2 partial pressure, the lower the onset temperature, which agrees with predictions of chemical thermodynamics. Fig. 5e demonstrates a decrease in the CO_2 uptake capacity over repeated cycles as a result of sintering and crystallisation

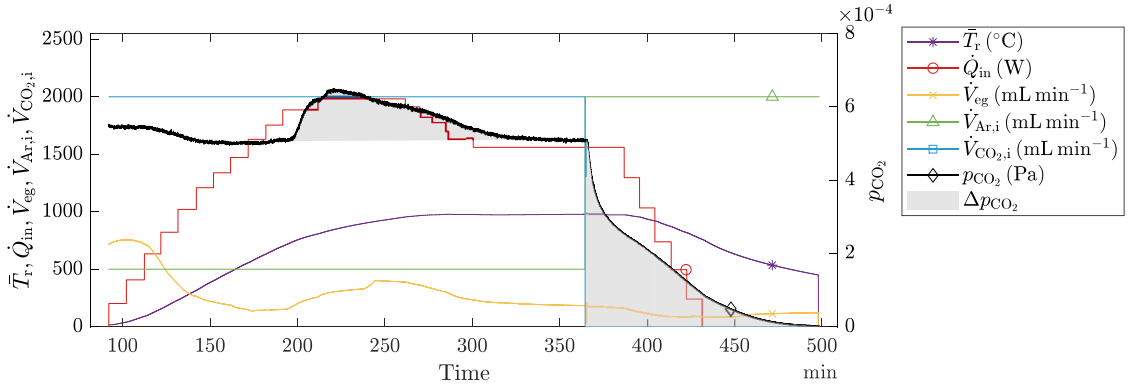

Fig. 6. Temporal changes of the average temperature inside the reactor reaction zone $\bar{T}_r$, the radiative power intercepted by the reactor aperture $\dot{Q}_{in}$, the volumetric flow rates of the exhaust gas flow, the supplied Ar and CO_2, $\dot{V}_{eg}$, $\dot{V}_{Ar,i}$, and $\dot{V}_{CO_2,i}$, respectively, and the partial pressure of CO_2 in the exhaust gases, p_{CO_2}, for the calcination reaction test (experimental run 1). The shaded regions denote the difference between the p_{CO_2} measured in the exhaust gases and p_{CO_2} in the supplied gases.

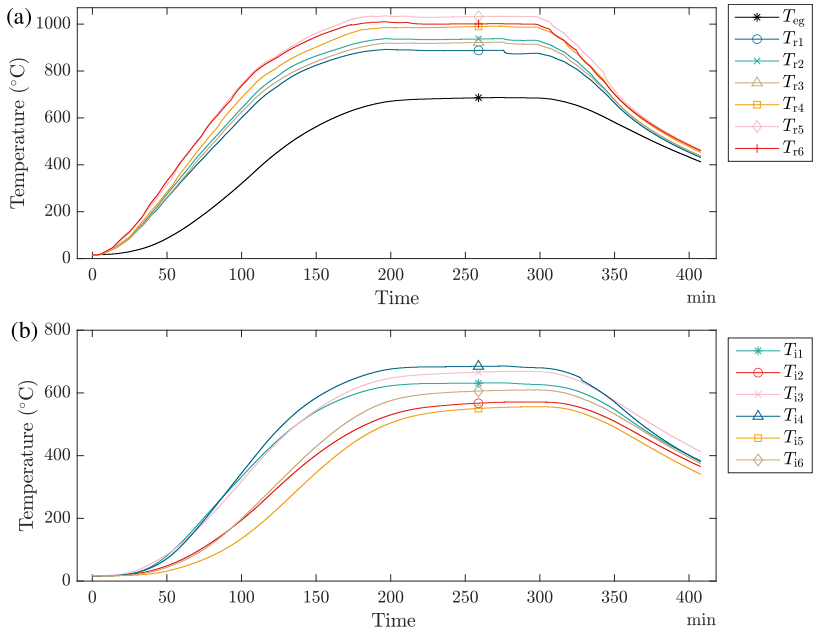

Fig. 7. Temporal temperatures (a) inside the reactor reaction zone, and (b) inside the insulation, for the calcination reaction test (experimental run 1).

of the particles outer layer during the calcination step. The reaction extent of carbonation decreases as the cycle proceeds. The CO_2 uptake capacity degrades over the eight cycles from 28.9 g CO_2 (69.4% of the theoretical 41.7 g CO_2) to a minimum of 10.0 g CO_2 (24.1%). Various approaches have been proposed in the literature to improve the material cyclability including steam addition [56], doping with other materials [85], and innovative sorbent precursors [86].

4.2. Case 1: A single calcination reaction step

For the calcination reaction test (experimental run 1), the volumetric flow rate of inlet sweeping gases is set at $\dot{V}_{CO_2,i} = 2,000\,\text{ml min}^{-1}$ and $\dot{V}_{Ar,i} = 500\,\text{ml min}^{-1}$. A sample of 800 g $CaCO_3$ particles is placed inside the reactor. The reactor is heated to a peak temperature of 1,035°C at an average heating rate of 6.5 K min^{-1}. It is then kept at this temperature until CO_2 generation from the $CaCO_3$ is not observed. Based on the TGA results (Section 4.1), a minimum calcination temperature of 920°C is identified for a relatively fast reaction rate. To mitigate the effect of temperature non-uniformity inside the packed bed, the reactor is heated to a peak temperature of 1,035°C such that the lowest measured temperature near the reactor aperture, T_{r1}, reached 920°C. The highest temperature T_{r5} is measured at the bottom of the annular reaction zone. During the cooling period, the purge gas is changed to pure Ar at a flow rate of 2,000 ml min^{-1} to avoid re-carbonation of the produced CaO. However, the $CaCO_3$ particles that did not decompose previously under higher CO_2 molar fraction due to a decrease in the CO_2 partial pressure, experience a second-stage calcination.

Fig. 6 shows the temporal changes of the maximum temperature inside the reaction zone, $T_{r,max}$, the radiative power intercepted by the reactor aperture, $\dot{Q}_{in}$, the partial pressure of CO_2 in the exhaust gases, p_{CO_2}, and the volumetric flow rates of exhaust gases, the supplied Ar and CO_2, $\dot{V}_{eg}$, $\dot{V}_{Ar,i}$ and $\dot{V}_{CO_2,i}$. The shaded regions in this figure correspond to periods when the measured CO_2 partial pressure deviates from the p_{CO_2} in the supplied gases, and they indicate the progress of the calcination reaction. As seen in this figure, the first-stage calcination reaction lasts for about 2 h under the purge gases of CO_2 and Ar mixture. Due to the switch of gas atmosphere to pure Ar, CO_2 partial pressure decreases and the calcination reaction proceeds further until it stops at about $t = 500$ min.

Fig. 7 shows the measured temperatures inside both the reactor reaction zone and the insulation. The temperature change follows the step-wise change in the radiative power input to the reactor. The maximum temperature difference of 160°C is found in the packed-bed particles. A higher temperature is found towards the bottom of the

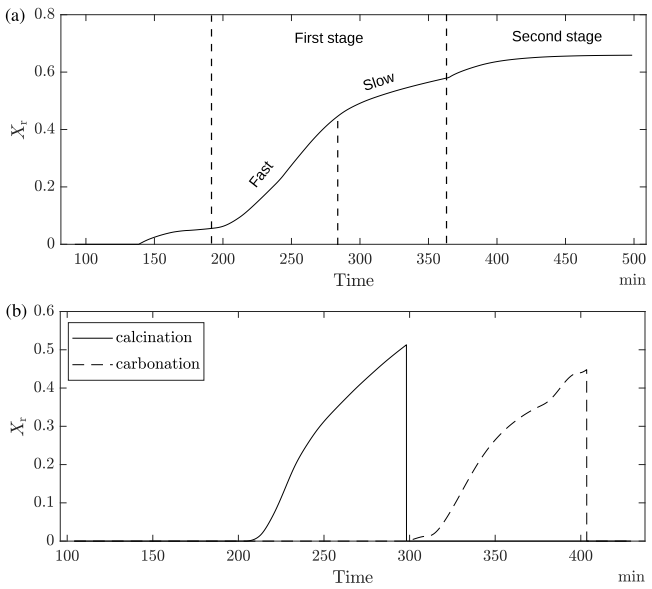

Fig. 8. Temporal reaction extent, X_r, for: (a) the calcination reaction test (experimental run 1), and (b) the one-cycle calcination–carbonation reaction test (experimental run 2).

reactor inner cavity (T_{r5} in Fig. 2), where the radiation directly hits the surface. The reactor is heated for 2 h and 18 min to reach the desired calcination temperature, above 920°C. Fig. 7b shows that the temperature inside the reactor insulation is in the range of approximately 550–690°C. The ratios of gas leakage before and after the reaction are found to be 0.73 and 0.82, respectively. Following the calculation procedures described in Section 3, the average solar-to-chemical conversion efficiency for the first-stage calcination is calculated to be approximately 5.3%. The extent of $CaCO_3$ calcination is calculated as a function of time as shown in Fig. 8a. The fast (chemical-controlled) and slow (diffusion-controlled) regimes are observed in this figure. The reaction extent of the first-stage calcination is approximately 0.58. This is followed by a further increment in the reaction extent to 0.66 during the change in the gas atmosphere from a mixture of CO_2 and Ar to pure Ar.

4.3. Case 2: A single calcination–carbonation cycle

Next, the reactor is tested for a single calcination–carbonation cycle (experimental run 2). Based on TGA results (see Section 4.1), the carbonation temperature T_{carb} is selected at around 800°C for the highest carbonation reaction extent with the average heating rate of 7.2 K min^{-1}. The purge gases are set at 20% CO_2 (625 ml min^{-1}) and 80% Ar (2,500 ml min^{-1}) during the calcination step, and 46.8% CO_2 (2,200 ml min^{-1}) and 53.2% Ar (2,500 ml min^{-1}) during the carbonation step. The flow rates and composition ratios of purge gases are not optimised in this work.

Fig. 9 shows the temporal changes of the maximum temperature inside the reaction zone, the radiative power intercepted by the reactor aperture, the volumetric flow rates of the exhaust gas, the supplied Ar and CO_2, and the partial pressure of CO_2 in the exhaust gases for experimental run 2. The deviation of p_{CO_2} from its value in the inlet gas stream—the shaded area in Fig. 9—indicates the occurrence of calcination (starting from about t = 200 min) and carbonation reactions. The reaction is switched to carbonation at about t = 298 min by reducing the radiative power input and increasing p_{CO_2} in the supplied gases. The gas leakage ratios before and after the reaction zone averaged for the entire experimental run 2 are found to be 0.42 and 0.88, respectively. The leakage ratio increases with the reactor temperature due to different expansion coefficients of the reactor materials at higher temperatures. The average solar-to-chemical conversion efficiency in this case is calculated to be approximately 8.6%. The reaction extents reach 0.51 and 0.45 at the end of calcination and carbonation steps as shown in Fig. 8b.

In this experiment, the maximum temperature difference inside the reaction zone is found to be 120°C during the calcination step. Although $T_{r,max}$ is set at 920°C during calcination (for the purpose of comparison with experimental run 1 where $T_{r,max}$ is set at 1,035°C), the majority of particles are below 920°C, which lowers the reaction extent as compared to that obtained in experimental run 1 (see 4.1). The fluctuation in p_{CO_2} observed during the carbonation step is a response to the variation in the reactor temperature. Due to the temperature difference in the reaction zone, particles undergo different reaction rates. As shown in Fig. 9, p_{CO_2} increases at around t = 330 min, as a result of the increase in the radiative power, $\dot{Q}_{in}$. This effect is possibly a result of a switch from the carbonation to calcination reaction in some particles.

4.4. Case 3: Multiple consecutive calcination–carbonation cycles

In this section, three reactor cycle tests are performed to investigate the effects of calcination duration on the reactor performance for the multiple consecutive calcination–carbonation cycles: (*i*) 1 h and 25 min (experimental run 3), (*ii*) 45 min (experimental run 4), and (*iii*) 30 min (experimental run 5). The purge gases are kept the same for both the calcination and carbonation reaction steps, i.e. 80% CO_2 (2,000 ml min^{-1}) and 20% Ar (500 ml min^{-1}). The peak calcination

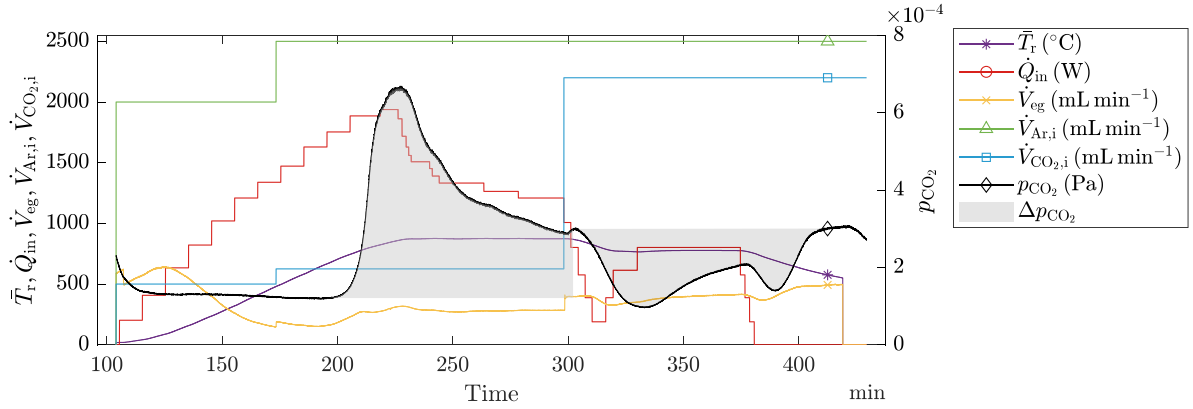

Fig. 9. Temporal changes of the average temperature inside the reactor reaction zone $\bar{T}_r$, the radiative power intercepted by the reactor aperture $\dot{Q}_{in}$, the volumetric flow rates of the exhaust gas, the supplied Ar and CO_2, $\dot{V}_{eg}$, $\dot{V}_{Ar,i}$, and $\dot{V}_{CO_2,i}$, respectively, and the partial pressure of CO_2 in the exhaust gases, p_{CO_2}, for the test of a single calcination–carbonation cycle (experimental run 2). The shaded regions denote the difference between p_{CO_2} measured in the exhaust gases and p_{CO_2} in the supplied gases.

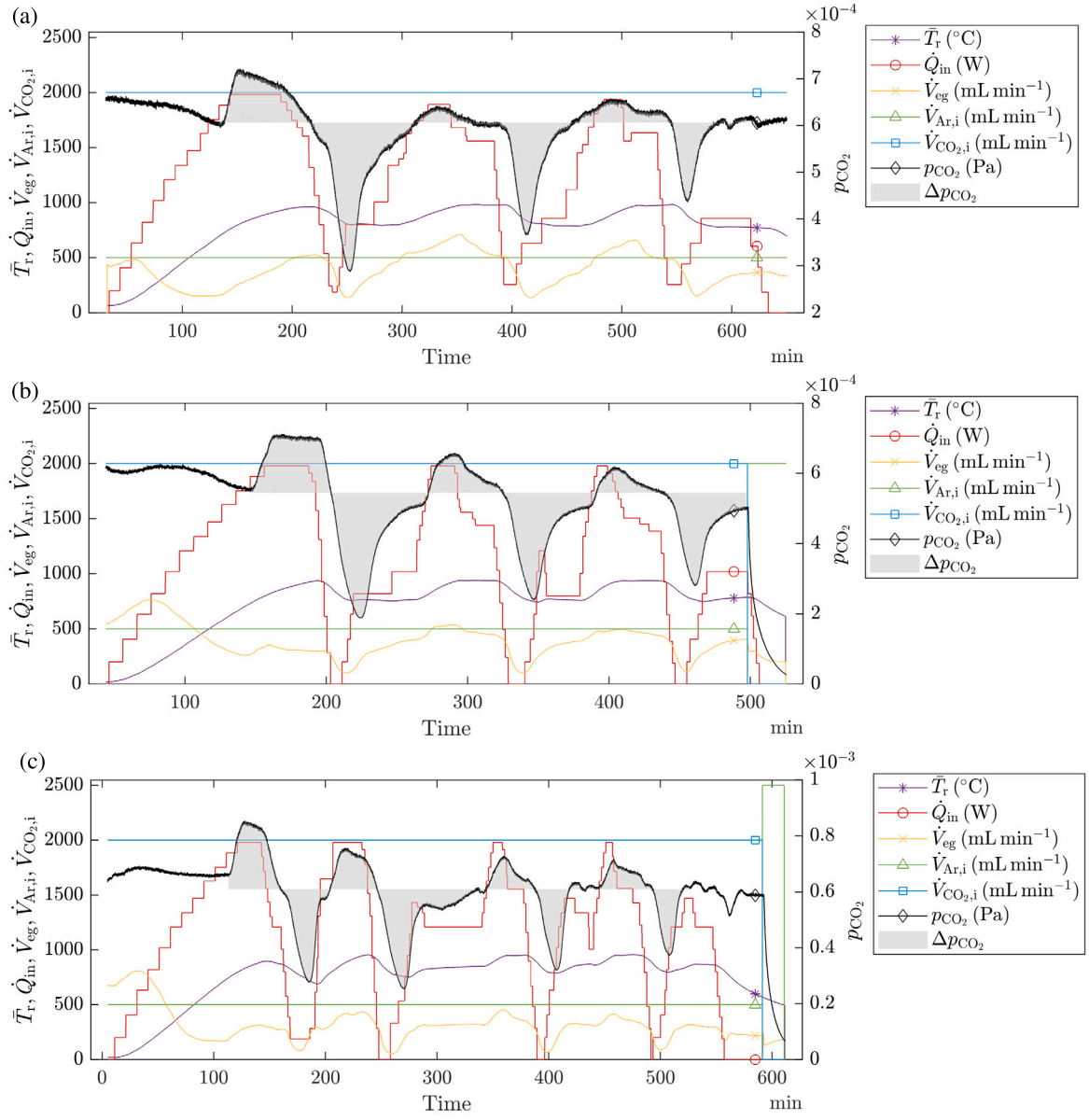

Fig. 10. Temporal changes of the average temperature inside the reactor reaction zone, $\bar{T}_r$, the radiative power intercepted by the reactor aperture, $\dot{Q}_{in}$, the volumetric flow rates of exhaust gas flow, supplied Ar and CO_2, $\dot{V}_{eg}$, $\dot{V}_{Ar,i}$, and $\dot{V}_{CO_2,i}$, respectively, and the partial pressure of CO_2 in the exhaust gases, p_{CO_2}, for tests of multiple consecutive calcination–carbonation cycles with calcination duration of: (a) 1 h and 25 min (experimental run 3), (b) 45 min (experimental run 4), and (c) 30 min (experimental run 5). The shaded regions denote the difference between p_{CO_2} measured in the exhaust gases and p_{CO_2} in the supplied gases.

temperature is increased to 1,020°C, such that the lowest temperature inside the reaction zone is above 920°C to ensure relatively faster calcination reaction kinetics as compared to experimental run 2. The reactor is kept at this peak temperature for about 10 min to complete the calcination reaction.

The results of these three tests are shown in Fig. 10. The average gas leakage ratios before the reaction zone are 0.83, 0.78, and 0.55 and after the reaction zone are 0.15, 0.55, and 0.80 for experimental runs 3, 4, and 5, respectively. The average heating rates for experimental runs 3, 4, and 5 are 5.1, 6.6, and 6.7 K min^{-1}. For the multi-cycle reaction tests, the average solar-to-chemical conversion efficiency is found to be approximately 1.3%, 2.8%, and 5.5% for experimental runs 3, 4, and 5, respectively. Since the reaction rate decreases with time during the calcination step, the solar-to-chemical conversion efficiency increases at a shorter duration of calcination step. A decrease in p_{CO_2} as time proceeds in experimental runs 3, 4, and 5 (see Fig. 10) indicates the degradation of material reactivity and CO_2 uptake capacity due to poor material cyclability. According to the measured flow rates of exhaust gases, the gas leakage ratios are transient. In particular, there is more gas leakage during the first cycle for all the three runs. In the process of heating the reactor from room temperature to T_{calc}, the gas leakage decreased first ($\dot{V}_{eg}$ increased as shown in Fig. 10), then increased and reached a relatively stabilised stage until the calcination reaction started. The released CO_2 from the calcination reaction led to an increase in $\dot{V}_{eg}$.

It is important to note that the measured calcination–carbonation reaction rates and extents in the reactor tests, as indicated by the peaks and trends of p_{CO_2}, do not represent the intrinsic kinetics of the reactions. The measured p_{CO_2} is affected by the chemical composition and morphology of the particles, and the particle temperatures. Due to the large number of particles present in the reactor and the non-uniformity of temperature distribution inside the reaction zone, the measured p_{CO_2} is the combined result of calcination–carbonation reactions proceeding

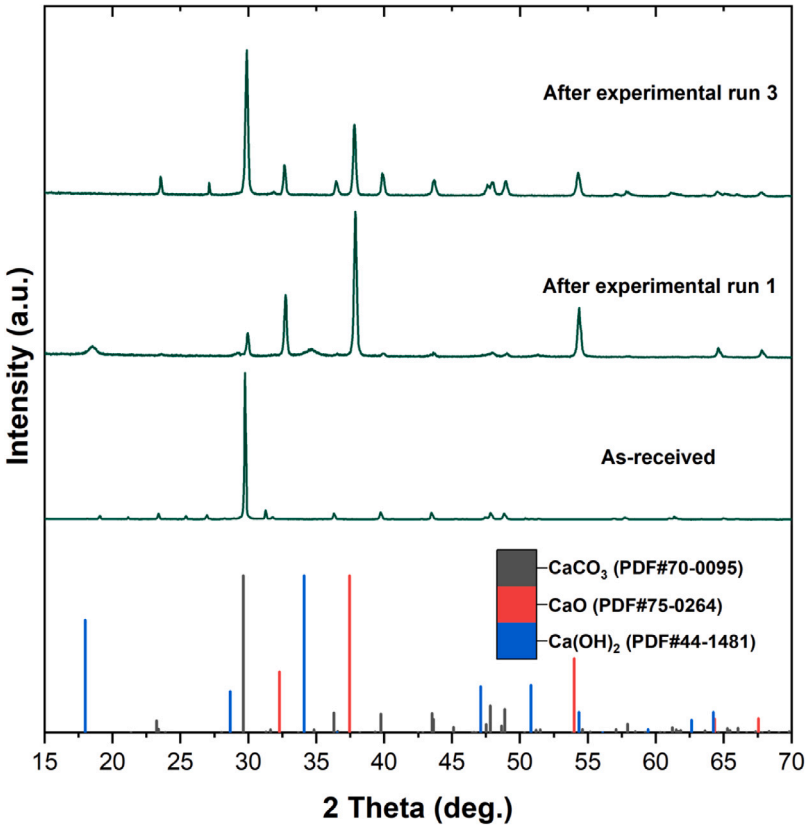

Fig. 11. XRD patterns for the calcium carbonate samples: as-received and after on-flux experimental runs 1 and 3.

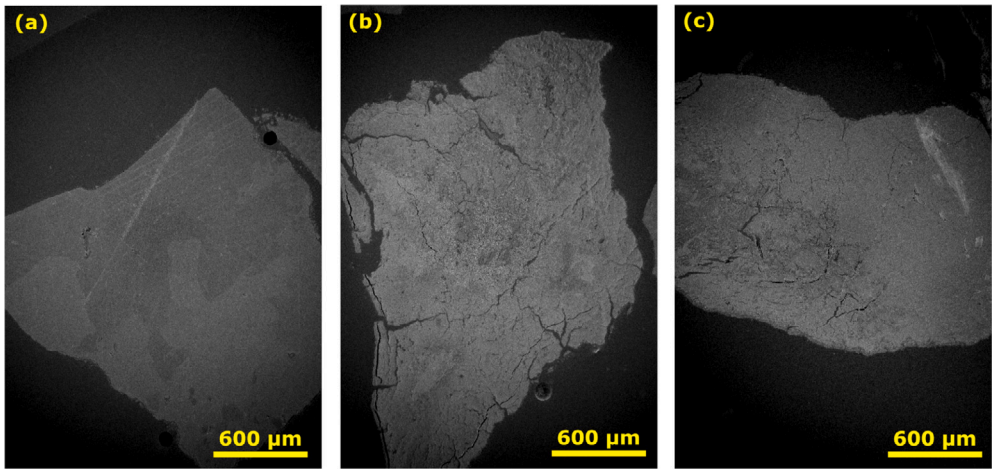

Fig. 12. Scanning electron microscopy images of samples (a) as-received, (b) after on-flux experimental run 1, and (c) after on-flux experimental run 3.

at different rates in the particles in the reaction zone, which differ from those obtained using thermogravimetric analyses.

4.5. Material characterisation results

X-ray diffraction (XRD) patterns of the samples as-received and after the experimental runs 1 and 3 are shown in Fig. 11. The XRD pattern of the as-received sample shows that all peaks are attributed to calcite ($CaCO_3$) as the main crystalline phase. For the particles after experimental run 1 (calcination test), the peaks identified by XRD analysis are attributed to $CaCO_3$, CaO, and $Ca(OH)_2$. $Ca(OH)_2$ is formed as a result of CaO reaction with moisture in air during particle cooling, storage and handling. After experimental run 3 (cycle test), the particles are mainly composed of $CaCO_3$ and a small amount of CaO.

SEM images of the polished samples are shown in Fig. 12. Particles after the calcination (see Fig. 12b) exhibit cracks compared to as-received particles (see Fig. 12a). These cracks are attributed to the escape of CO_2 from the particles and volume reduction during calcination, which is in line with the data reported in the literature [12,87]. In contrast, Fig. 12c shows that the cracks near the surface of the particles are closed after the carbonation, while the inner part of the particle remains cracked. This indicates that the carbonation reaction primarily

occurs at the particle surface. After $CaCO_3$ is formed, it is hard for CO_2 to further penetrate into the particle—a key factor limiting the cyclability of the material.

4.6. Lessons learned

The first-of-its kind packed-bed reactor prototype evaluated in this study has several conceptual advantages over other solar reactor designs pertaining to cyclic chemical looping processes with gas–solid reactions. It allows for the realisation of the solar-driven calcination–carbonation cycle in a single reactor without any moving parts while transport of solids is mitigated, which in turn allows for the reduction of material and energy losses and for simplifying the reactor operation. Design shortcomings of the current prototype have also been identified and are recommended for addressing in future research.

The disparate thermo-mechanical characteristics of the ceramic and metallic parts have resulted in breaking the high-temperature sealings around the reaction zone, which in turn led to considerable gas leaks. Filling and removing the solid reactants during tests of the research-grade reactor proved to be challenging and impractical due to many steps in the reactor assembly and disassembly processes. Improved designs are required to handle the solid reactant replacement, for example to compensate for the loss of reactant reactivity after multiple cycles.

For industrial-scale operation of such a reactor, the large amount of the solid reactant stored in the reactor may result in an excessively large reactor size and ineffective heat transfer to and from the reaction zone. The reactor performance can be improved by introducing heat-conducting and particle-stabilising fins in the annular reaction zone to prevent particle displacing due to large gas flow rates and particle size change during particle thermo-mechanical disintegration and chemical reactions. The fins will allow for reducing the temperature non-uniformity observed in the reaction zone of the current prototype.

Finally, industrial-scale operation of a single reactor realising the calcination–carbonation cycle may be impractical and inefficient due to solar "iddle" times during the carbonation reaction periods. Two- and multiple-reactor configurations developed for other thermochemical cycles can be possibly adapted to the calcination–carbonation cycle [71, 72].

5. Summary and conclusions

This work has presented the first cyclic calcination–carbonation process demonstrated in a solar packed-bed reactor. The two-step CaO-based calcination–carbonation cycle was studied for solar-driven CO_2 capture and thermochemical energy storage applications. The 2-kW_{th} indirectly-irradiated packed-bed solar thermochemical reactor was evaluated under high-flux solar-simulator irradiation. The operating conditions for the reactor experiments were designed based on results obtained using a thermogravimetric analysis (TGA) with the same sample material of natural calcium carbonate particles. The reactor was tested for three cases: (*i*) a calcination reaction, (*ii*) one-cycle calcination–carbonation reactions, and (*iii*) multi-cycle calcination–carbonation reactions. The material samples as received and after on-flux experimental runs were characterised using scanning electron microscopy (SEM) and X-ray diffraction (XRD).

The natural calcium carbonate particles was found to have good mechanical stability but unsatisfactory chemical performance in the cyclic operation. The temperature difference inside the reaction zone during the three tests was in the range 80–160°C, which presents a challenge for the reactor scale-up with the present design. The average solar-to-chemical energy conversion efficiency was between 1.4% and 8.8%.

The first-of-its kind packed-bed reactor prototype evaluated in this study has several conceptual advantages over other solar reactor designs pertaining to cyclic chemical looping processes with gas–solid reactions. It allows for the realisation of the solar-driven calcination–carbonation cycle in a single reactor without any moving parts while transport of solids is mitigated, which in turn allows for the reduction of material and energy losses and for simplifying the reactor operation. However, several reactor design shortcomings have been identified and are recommended for addressing in future research. The thermo-mechanical compatibility of materials and parts requires further considerations along with a solution to stabilise particles and enhance heat transfer in the reaction zone to mitigate temperature non-uniformity and consequently non-uniform reaction rates. The latter is critical for designing efficient large-scale reactors closely matching the duration of the calcination–carbonation cycle steps to the periods of solar irradiation.

Declaration of competing interest

The authors declare that they have no known competing financial interests or personal relationships that could have appeared to influence the work reported in this paper.

Data availability

Data will be made available on request

Acknowledgements

We thank David Tychsen-Smith, Colin Carvolth, Kevin Carvolth, Erasmo Scipione, and Jason Chen for their technical support with the experiments; Johannes Pottas and Mustafa Habib for the optical alignment and radiometry flux characterisation of the high-flux solar simulator; and Luke Melmoth, Robert Gresham, and Roman Bader for their contributions to the solar reactor design and analysis.

Funding

This research was funded by the Australian Solar Thermal Research Institute, a project supported by the Australian Government through the Australian Renewable Energy Agency (1-SRI002). Leanne Matthews was supported by the U.S. National Science Foundation Graduate Research Fellowship (Grant No. 00006595).

References

[1] L. Reich, L. Yue, R. Bader, W. Lipiński, Towards solar thermochemical carbon dioxide capture via calcium oxide looping: A review, Aerosol Air Qual. Res. 14 (2) (2014) 500–514, http://dx.doi.org/10.4209/aaqr.2013.05.0169.

[2] P. Fennell, B. Anthony (Eds.), Calcium and Chemical Looping Technology for Power Generation and Carbon Dioxide (CO_2) Capture, in: Woodhead Publishing Series in Energy, Woodhead Publishing, Cambridge, 2015.

[3] S. Pascual, P. Lisbona, M. Bailera, L.M. Romeo, Design and operational performance maps of calcium looping thermochemical energy storage for concentrating solar power plants, Energy 220 (2021) 119715, http://dx.doi.org/10.1016/j.energy.2020.119715.

[4] C. Ortiz, J.M. Valverde, R. Chacartegui, L.A. Perez-Maqueda, P. Giménez, The calcium-looping ($CaCO_3$/CaO) process for thermochemical energy storage in concentrating solar power plants, Renew. Sustain. Energy Rev. 113 (2019) 109252, http://dx.doi.org/10.1016/j.rser.2019.109252.

[5] W. Liu, H. An, C. Qin, J. Yin, G. Wang, B. Feng, M. Xu, Performance enhancement of calcium oxide sorbents for cyclic CO_2 capture: A review, Energy Fuels 26 (5) (2012) 2751–2767, http://dx.doi.org/10.1021/ef300220x.

[6] J. Liu, Y. Xuan, L. Teng, Q. Zhu, X. Liu, Y. Ding, Solar-driven calcination study of a calcium-based single particle for thermochemical energy storage, Chem. Eng. J. 450 (2022) 138140, http://dx.doi.org/10.1016/j.cej.2022.138140.

[7] J.A.H. Oates, Lime and Limestone: Chemistry and Technology, Production and Uses, Wiley-VCH, Weinheim, 1998, http://dx.doi.org/10.1002/9783527612024.

[8] E. Bagherisereshki, J. Tran, F. Lei, N. AuYeung, Investigation into SrO/$SrCO_3$ for high temperature thermochemical energy storage, Sol. Energy 160 (2018) 85–93, http://dx.doi.org/10.1016/j.solener.2017.11.073.

[9] L. André, S. Abanades, Evaluation and performances comparison of calcium, strontium and barium carbonates during calcination/carbonation reactions for solar thermochemical energy storage, J. Energy Storage 13 (2017) 193–205, http://dx.doi.org/10.1016/j.est.2017.07.014.

[10] L. Imponenti, K.J. Albrecht, J.W. Wands, M.D. Sanders, G.S. Jackson, Thermochemical energy storage in strontium-doped calcium manganites for concentrating solar power applications, Sol. Energy 151 (2017) 1–13, http://dx.doi.org/10.1016/j.solener.2017.05.010.

[11] A. Bayon, R. Bader, M. Jafarian, L. Fedunik-Hofman, Y. Sun, J. Hinkley, S. Miller, W. Lipiński, Techno-economic assessment of solid–gas thermochemical energy storage systems for solar thermal power applications, Energy 149 (2018) 473–484, http://dx.doi.org/10.1016/j.energy.2017.11.084.

[12] L. Yue, W. Lipiński, Thermal transport model of a sorbent particle undergoing calcination–carbonation cycling, AIChE J. 61 (8) (2015) 2647–2656, http://dx.doi.org/10.1002/aic.14840.

[13] M. Benitez-Guerrero, J.M. Valverde, P.E. Sanchez-Jimenez, A. Perejon, L.A. Perez-Maqueda, Multicycle activity of natural $CaCO_3$ minerals for thermochemical energy storage in concentrated solar power plants, Sol. Energy 153 (2017) 188–199, http://dx.doi.org/10.1016/j.solener.2017.05.068.

[14] L. Fedunik-Hofman, A. Bayon, S.W. Donne, Comparative kinetic analysis of $CaCO_3$/CaO reaction system for energy storage and carbon capture, Appl. Sci. 9 (21) (2019) 4601, http://dx.doi.org/10.3390/app9214601.

[15] L. Fedunik-Hofman, A. Bayon, J. Hinkley, W. Lipiński, S.W. Donne, Friedman method kinetic analysis of CaO-based sorbent for high-temperature thermochemical energy storage, Chem. Eng. Sci. 200 (2019) 236–247, http://dx.doi.org/10.1016/j.ces.2019.02.003.

[16] J. Arcenegui-Troya, P.E. Sánchez-Jiménez, A. Perejón, J.M. Valverde, R. Chacartegui, L.A. Pérez-Maqueda, Calcium-looping performance of biomineralized $CaCO_3$ for CO_2 capture and thermochemical energy storage, Ind. Eng. Chem. Res. 59 (29) (2020) 12924–12933, http://dx.doi.org/10.1021/acs.iecr.9b05997.

[17] L. Yue, A. Bayon, W. Lipiński, Thermal transport and chemical conversion in single reacting sorbent particles, AIChE J. 67 (2021) e17267, http://dx.doi.org/10.1002/aic.17267.

[18] H. Zheng, X. Liu, Y. Xuan, C. Song, D. Liu, Q. Zhu, Z. Zhu, K. Gao, Y. Li, Y. Ding, Thermochemical heat storage performances of fluidized black $CaCO_3$ pellets under direct concentrated solar irradiation, Renew. Energy 178 (2021) 1353–1369, http://dx.doi.org/10.1016/j.renene.2021.07.026.

[19] M. Silakhori, M. Jafarian, A. Chinnici, W. Saw, M. Venkataraman, W. Lipiński, G. Nathan, Effects of steam on the kinetics of calcium carbonate calcination, Chem. Eng. Sci. (2021) 116987, http://dx.doi.org/10.1016/j.ces.2021.116987.

[20] W. Lipiński, A. Steinfeld, Transient radiative heat transfer within a particle suspension undergoing endothermal decomposition—shrinking vs. non-shrinking particles, in: M.P. Mengüç, N. Selçuk (Eds.), Proceedings of the 4th International Symposium on Radiative Transfer RAD-IV, 2004, pp. 305–314, http://dx.doi.org/10.1615/ICHMT.2004.RAD-4.300.

[21] W. Lipiński, A. Steinfeld, Heterogeneous thermochemical decomposition under direct irradiation, Int. J. Heat Mass Transfer 47 (8–9) (2004) 1907–1916, http://dx.doi.org/10.1016/j.ijheatmasstransfer.2003.10.010.

[22] P.P. Ebner, W. Lipiński, Heterogeneous thermochemical decomposition of a semi-transparent particle under direct irradiation, Chem. Eng. Sci. 66 (12) (2011) 2677–2689, http://dx.doi.org/10.1016/j.ces.2011.03.028.

[23] P.P. Ebner, W. Lipiński, Heterogeneous thermochemical decomposition of a semi-transparent particle under high-flux irradiation—Changing grain size vs. shrinking core models, Numer. Heat Transfer A 62 (5) (2012) 412–431, http://dx.doi.org/10.1080/10407782.2012.703466.

[24] P.P. Ebner, W. Lipiński, Heterogeneous thermochemical decomposition of a semi-transparent particle under high-flux irradiation—Uniform vs. non-uniform irradiation, Heat Mass Transf. 50 (7) (2014) 1031–1036, http://dx.doi.org/10.1007/s00231-014-1311-7.

[25] L. Yue, W. Lipiński, A numerical model of transient thermal transport phenomena in a high-temperature solid–gas reacting system for CO_2 capture applications, Int. J. Heat Mass Transfer 85 (2015) 1058–1068, http://dx.doi.org/10.1016/j.ijheatmasstransfer.2015.01.124.

[26] L. Dombrovsky, W. Lipiński, Transient temperature and thermal stress profiles in semi-transparent particles under high-flux irradiation, Int. J. Heat Mass Transfer 50 (11–12) (2007) 2117–2123, http://dx.doi.org/10.1016/j.ijheatmasstransfer.2006.11.008.

[27] L. Yue, L. Reich, T. Simon, R. Bader, W. Lipiński, Progress in thermal transport modeling of carbonate-based reacting systems, Internat. J. Numer. Methods Heat Fluid Flow 27 (5) (2017) 1098–1107, http://dx.doi.org/10.1108/HFF-03-2016-0087.

[28] W.N.R. Wan Isahak, Z.A. Che Ramli, M.W. Mohamed Hisham, M.A. Yarmo, The formation of a series of carbonates from carbon dioxide: Capturing and utilisation, Renew. Sustain. Energy Rev. 47 (2015) 93–106, http://dx.doi.org/10.1016/j.rser.2015.03.020.

[29] B. Dou, C. Wang, Y. Song, H. Chen, B. Jiang, M. Yang, Y. Xu, Solid sorbents for in-situ CO_2 removal during sorption-enhanced steam reforming process: A review, Renew. Sustain. Energy Rev. 53 (2016) 536–546, http://dx.doi.org/10.1016/j.rser.2015.08.068.

[30] A. Bayon, A.J. Carrillo, E. Mastronardo, J.M. Coronado, Thermochemical heat storage at high temperature, in: W. Lipiński (Ed.), Advances in Chemical Engineering, Vol. 58, Academic Press, 2021, pp. 247–295, http://dx.doi.org/10.1016/bs.ache.2021.10.004.

[31] J.P. Rincon Duarte, D. Kriechbaumer, B. Lachmann, S. Tescari, T. Fend, M. Roeb, C. Sattler, Solar calcium looping cycle for CO_2 capturing in a cement plant. definition of process parameters and reactors selection, Sol. Energy 238 (15) (2022) 189–202, http://dx.doi.org/10.1016/j.solener.2022.04.031.

[32] C. Tregambi, F. Montagnaro, P. Salatino, R. Solimene, A model of integrated calcium looping for CO_2 capture and concentrated solar power, Sol. Energy 120 (2015) 208–220, http://dx.doi.org/10.1016/j.solener.2015.07.017.

[33] R. Chacartegui, A. Alovisio, C. Ortiz, J.M. Valverde, V. Verda, J.A. Becerra, Thermochemical energy storage of concentrated solar power by integration of the calcium looping process and a CO_2 power cycle, Appl. Energy 173 (2016) 589–605, http://dx.doi.org/10.1016/j.apenergy.2016.04.053.

[34] C. Ortiz, M.C. Romano, J.M. Valverde, M. Binotti, R. Chacartegui, Process integration of calcium-looping thermochemical energy storage system in concentrating solar power plants, Energy 155 (2018) 535–551, http://dx.doi.org/10.1016/j.energy.2018.04.180.

[35] Y. Deng, J. Liu, S. Li, R. Dewil, H. Zhang, J. Baeyens, H. Mikulčić, The steam-assisted calcination of limestone and dolomite for energy savings and to foster solar calcination processes, J. Clean. Prod. 363 (2022) 132640, http://dx.doi.org/10.1016/j.jclepro.2022.132640.

[36] Q. Gong, H. Shi, Y. Chai, R. Yu, A. Weisenburger, D. Wang, A. Bonk, T. Bauer, W. Ding, Molten chloride salt technology for next-generation CSP plants: Compatibility of fe-based alloys with purified molten $MgCl_2$-KCl-NaCl salt at 700°C, Appl. Energy 324 (2022) 119708, http://dx.doi.org/10.1016/j.apenergy.2022.119708.

[37] L. Li, J. Coventry, R. Bader, J. Pye, W. Lipiński, Optics of solar central receiver systems: a review, Opt. Express 24 (14) (2016) A985–A1007, http://dx.doi.org/10.1364/OE.24.00A985.

[38] G. Levêque, R. Bader, W. Lipiński, S. Haussener, High-flux optical systems for solar thermochemistry, Sol. Energy 156 (2017) 133–148, http://dx.doi.org/10.1016/j.solener.2017.07.046.

[39] L. Li, B. Wang, R. Bader, T. Cooper, W. Lipiński, Concentrating collector systems for solar thermal and thermochemical applications, in: W. Lipiński (Ed.), Advances in Chemical Engineering, Vol. 58, Academic Press, 2021, pp. 1–53, http://dx.doi.org/10.1016/bs.ache.2021.10.001.

[40] M.B. Venkataraman, A. Rahbari, P. van Eyk, A.W. Weimer, W. Lipiński, J. Pye, Liquid fuel production via supercritical water gasification of algae: a role for solar heat integration? Sustain Energy Fuels 5 (2021) 6269–6297, http://dx.doi.org/10.1039/d1se01615f.

[41] X. Wang, F. Zhang, L. Li, H. Zhang, S. Deng, Carbon dioxide capture, in: W. Lipiński (Ed.), Advances in Chemical Engineering, Vol. 58, Academic Press, 2021, pp. 297–348, http://dx.doi.org/10.1016/bs.ache.2021.10.005.

[42] V. Nikulshina, C. Gebald, A. Steinfeld, CO_2 capture from atmospheric air via consecutive CaO-carbonation and $CaCO_3$-calcination cycles in a fluidized-bed solar reactor, Chem. Eng. J. 146 (2) (2009) 244–248, http://dx.doi.org/10.1016/j.cej.2008.06.005.

[43] L. Fedunik-Hofman, A. Bayon, X. Gao, A. Tricoli, S.W. Donne, Dysprosium oxide-supported CaO for thermochemical energy storage, Front. Mater. 8 (2021) 670638, http://dx.doi.org/10.3389/fmats.2021.670638.

[44] G. Moumin, S. Tescari, P. Sundarraj, L. de Oliveira, M. Roeb, C. Sattler, Solar treatment of cohesive particles in a directly irradiated rotary kiln, Sol. Energy 182 (2019) 480–490, http://dx.doi.org/10.1016/j.solener.2019.01.093.

[45] T. Esence, E. Guillot, M. Tessonneaud, J.-L. Sans, G. Flamant, Solar calcination at pilot scale in a continuous flow multistage horizontal fluidized bed, Sol. Energy 207 (2020) 367–378, http://dx.doi.org/10.1016/j.solener.2020.06.098.

[46] M. Tomatis, H.K. Jeswani, L. Stamford, A. Azapagic, Assessing the environmental sustainability of an emerging energy technology: Solar thermal calcination for cement production, Sci. Total Environ. 742 (2020) 140510, http://dx.doi.org/10.1016/j.scitotenv.2020.140510.

[47] D. Yadav, R. Banerjee, A review of solar thermochemical processes, Renew. Sustain. Energy Rev. 54 (2016) 497–532, http://dx.doi.org/10.1016/j.rser.2015.10.026.

[48] W. Lipiński, E. Abbasi-Shavazi, J. Chen, J. Coventry, M. Hangi, S. Iyer, A. Kumar, L. Li, S. Li, J. Pye, J.F. Torres, B. Wang, Y. Wang, V.M. Wheeler, Progress in heat transfer research for high-temperature solar thermal applications, Appl. Therm. Eng. 184 (2021) 116137, http://dx.doi.org/10.1016/j.applthermaleng.2020.116137.

[49] W. Lipiński (Ed.), Solar Thermochemistry, in: Advances in Chemical Engineering, vol. 58, Academic Press, Cambridge, MA, 2021, URL https://www.elsevier.com/books/solar-thermochemistry/lipinski/978-0-12-820647-8.

[50] W. Lipiński, J.H. Davidson, S. Haussener, J.F. Klausner, A.M. Mehdizadeh, J. Petrasch, A. Steinfeld, L. Venstrom, Review of heat transfer research for solar thermochemical applications, J. Thermal Sci. Eng. Appl. 5 (2) (2013) 021005, http://dx.doi.org/10.1115/1.4024088.

[51] G. Zsembinszki, A. Solé, C. Barreneche, C. Prieto, A. Fernández, L. Cabeza, Review of reactors with potential use in thermochemical energy storage in concentrated solar power plants, Energies 11 (9) (2018) 2358, http://dx.doi.org/10.3390/en11092358.

[52] B. Wang, A. Rahbari, M. Hangi, X. Li, C.-H. Wang, W. Lipiński, Topological and hydrodynamic analyses of solar thermochemical reactors for aerodynamic-aided window protection, Eng. Appl. Comput. Fluid Mech. 16 (1) (2022) 1195–1210, http://dx.doi.org/10.1080/19942060.2022.2078883.

[53] L. Reich, L. Melmoth, L. Yue, R. Bader, R. Gresham, T. Simon, W. Lipiński, A solar reactor design for research on calcium oxide-based carbon dioxide capture, J. Solar Energy Eng. 139 (5) (2017) 054501, http://dx.doi.org/10.1115/1.4037089.

[54] L. Reich, Design and modeling of a solar reactor for thermochemical carbon dioxide capture (Ph.D. thesis), University of Minnesota, 2015, URL https://hdl.handle.net/11299/175312.

[55] G. Flamant, D. Hernandez, C. Bonet, J.-P. Traverse, Experimental aspects of the thermochemical conversion of solar energy—Decarbonation of $CaCO_3$, Sol. Energy 24 (4) (1980) 385–395, http://dx.doi.org/10.1016/0038-092X(80)90301-1.

[56] C. Tregambi, P. Salatino, R. Solimene, F. Montagnaro, An experimental characterization of calcium looping integrated with concentrated solar power, Chem. Eng. J. 331 (2018) 794–802, http://dx.doi.org/10.1016/j.cej.2017.08.068.

[57] F. Di Lauro, C. Tregambi, F. Montagnaro, P. Salatino, R. Chirone, R. Solimene, Improving the performance of calcium looping for solar thermochemical energy storage and CO_2 capture, Fuel 298 (2021) 120791, http://dx.doi.org/10.1016/j.fuel.2021.120791.

[58] S. Padula, C. Tregambi, R. Solimene, R. Chirone, M. Troiano, P. Salatino, A novel fluidized bed "thermochemical battery"for energy storage in concentrated solar thermal technologies, Energy Convers. Manage. 236 (2021) 113994, http://dx.doi.org/10.1016/j.enconman.2021.113994.

[59] A. Steinfeld, A. Imhof, D. Mischler, Experimental investigation of an atmospheric-open cyclone solar reactor for solid–gas thermochemical reactions, J. Solar Energy Eng. 114 (3) (1992) 171–174, http://dx.doi.org/10.1115/1.2930001.

[60] A. Meier, E. Bonaldi, G.M. Cella, W. Lipiński, D. Wuillemin, R. Palumbo, Design and experimental investigation of a horizontal rotary reactor for the solar thermal production of lime, Energy 29 (5) (2004) 811–821, http://dx.doi.org/10.1016/S0360-5442(03)00187-7.

[61] S. Abanades, L. André, Design and demonstration of a high temperature solar-heated rotary tube reactor for continuous particles calcination, Appl. Energy 212 (2018) 1310–1320, http://dx.doi.org/10.1016/j.apenergy.2018.01.019.

[62] A. Imhof, Decomposition of limestone in a solar reactor, Renew. Energy 10 (1997) 239–246, http://dx.doi.org/10.1016/0960-1481(96)00072-9.

[63] A. Meier, E. Bonaldi, G.M. Cella, W. Lipiński, Multitube rotary kiln for the industrial solar production of lime, J. Solar Energy Eng. 127 (3) (2005) 386–395, http://dx.doi.org/10.1115/1.1979517.

[64] A. Meier, E. Bonaldi, G.M. Cella, W. Lipiński, D. Wuillemin, Solar chemical reactor technology for industrial production of lime, Sol. Energy 80 (10) (2006) 1355–1362, http://dx.doi.org/10.1016/j.solener.2005.05.017.

[65] R.B. Diver, J.E. Miller, M.D. Allendorf, N.P. Siegel, R.E. Hogan, Solar thermochemical water-splitting ferrite-cycle heat engines, J. Solar Energy Eng. 130 (4) (2008) 041001, http://dx.doi.org/10.1115/1.2969781.

[66] R. Diver, J. Miller, N. Siegel, T. Moss, Testing of a CR5 solar thermochemical heat engine prototype, in: Proceedings of the ASME 2010 4th International Conference on Energy Sustainability, 2010, pp. 97–104, http://dx.doi.org/10.1115/ES2010-90093.

[67] J. Lapp, J.H. Davidson, W. Lipiński, Heat transfer analysis of a solid–solid heat recuperation system for solar-driven nonstoichiometric redox cycles, J. Solar Energy Eng. 135 (3) (2013) 031004, http://dx.doi.org/10.1115/1.4023357.

[68] J. Lapp, W. Lipiński, Transient three-dimensional heat transfer model of a solar thermochemical reactor for H_2O and CO_2 splitting via nonstoichiometric ceria redox cycling, J. Solar Energy Eng. 136 (3) (2014) 031006, http://dx.doi.org/10.1115/1.4026465.

[69] R. Bader, R. Bala Chandran, L.J. Venstrom, S.J. Sedler, P.T. Krenzke, R.M. De Smith, A. Banerjee, T.R. Chase, J.H. Davidson, W. Lipiński, Design of a solar reactor to split CO_2 via isothermal redox cycling of ceria, J. Solar Energy Eng. 137 (3) (2015) 031007, http://dx.doi.org/10.1115/1.4028917.

[70] R. Bala Chandran, R. Bader, W. Lipiński, Transient heat and mass transfer analysis in a porous ceria structure of a novel solar redox reactor, Int. J. Therm. Sci. 92 (2015) 138–149, http://dx.doi.org/10.1016/j.ijthermalsci.2015.01.016.

[71] S. Yang, L. Li, B. Wang, S. Li, J. Wang, P. Lund, W. Lipiński, Thermodynamic analysis of a conceptual fixed-bed solar thermochemical cavity receiver–reactor array for water splitting via ceria redox cycling, Front. Energy Res. 9 (2021) 565761, http://dx.doi.org/10.3389/fenrg.2021.565761.

[72] R. Schäppi, D. Rutz, F. Dähler, A. Muroyama, P. Haueter, J. Lilliestam, A. Patt, P. Furler, A. Steinfeld, Drop-in fuels from sunlight and air, Nature 601 (7891) (2022) 63–68, http://dx.doi.org/10.1038/s41586-021-04174-y.

[73] A.S. Patankar, X.-Y. Wu, W. Choi, H.L. Tuller, A.F. Ghoniem, A reactor train system for efficient solar thermochemical fuel production, J. Solar Energy Eng. 144 (6) (2022) 061014, http://dx.doi.org/10.1115/1.4055298.

[74] L. Melmoth, Designing a solar thermochemical reactor for carbon dioxide capture, (Honours thesis), The Australian National University, 2014.

[75] L. Reich, R. Bader, T.W. Simon, W. Lipiński, Thermal transport model of a packed-bed reactor for solar thermochemical CO_2 capture, Special Top. Rev. Porous Media 6 (2) (2015) 197–209, http://dx.doi.org/10.1615/.2015012344.

[76] R. Bader, S. Haussener, W. Lipiński, Optical design of multisource high-flux solar simulators, J. Solar Energy Eng. 137 (2) (2015) 021012, http://dx.doi.org/10.1115/1.4028702.

[77] G. Levêque, R. Bader, W. Lipiński, S. Haussener, Experimental and numerical characterization of a new 45 kW_e multi-source high-flux solar simulator, Opt. Express 24 (22) (2016) A1360–A1373, http://dx.doi.org/10.1364/OE.24.0A1360.

[78] J. Pottas, L. Li, M. Habib, C.-H. Wang, J. Coventry, W. Lipiński, Optical alignment and radiative flux characterization of a multi-source high-flux solar simulator, Sol. Energy 236 (1) (2022) 434–444, http://dx.doi.org/10.1016/j.solener.2022.02.026.

[79] R. Bader, G. Levêque, S. Haussener, W. Lipiński, High-flux solar simulator technology, in: Proceedings of the OSA 2016 Light, Energy and the Environment Congress, Optical Society of America, Leipzig, 2016, http://dx.doi.org/10.1364/OSE.2016.SoM3C.3, SoM3C–3.

[80] User's manual: QMS 100 series gas analyzer, 2021, URL https://www.thinksrs.com/downloads/pdfs/manuals/QMSm.pdf, Retrieved on 16 August 2021.

[81] M. Habib, Control system design for a solar receiver-reactor, The Australian National University, 2019, http://dx.doi.org/10.25911/5dfc95731561a.

[82] Omya Australia Pty Limited, URL https://www.omya.com/au-en, Retrieved on 16 August 2021.

[83] M. Binnewies, E. Milke, Thermochemical Data of Elements and Compounds, second ed., Wiley-VCH, Weinheim, 2002, http://dx.doi.org/10.1002/9783527618347.

[84] Y.S. Touloukian, R.W. Powell, C.Y. Ho, P.G. Klemens (Eds.), Thermal conductivity—Nonmetallic solids, in: Thermophysical Properties of Matter, vol. 2, IFI/Plenum, New York, 1970.

[85] T.X. Xu, X.K. Tian, A.A. Khosa, J. Yan, Q. Ye, C.Y. Zhao, Reaction performance of $CaCO_3$/CaO thermochemical energy storage with TiO_2 dopant and experimental study in a fixed-bed reactor, Energy 236 (2021) 121451, http://dx.doi.org/10.1016/j.energy.2021.121451.

[86] F.-C. Yu, N. Phalak, Z. Sun, L.-S. Fan, Activation strategies for calcium-based sorbents for CO_2 capture: A perspective, Ind. Eng. Chem. Res. 51 (4) (2012) 2133–2142, http://dx.doi.org/10.1021/ie200802y.

[87] C. Herce, S. Stendardo, C. Cortés, Increasing CO_2 carrying capacity of dolomite by means of thermal stabilization by triggered calcination, Chem. Eng. J. 262 (2015) 18–28, http://dx.doi.org/10.1016/j.cej.2014.09.076.